



Postconstruction Deformation Characteristics of High-Fill Foundations of Kunming Changshui International Airport Using Time-Series InSAR Technology

Mingchun Wen , Mengshi Yang , *Member, IEEE*, Xin Zhao , and Zhifang Zhao 

Abstract—The Kunming Changshui International Airport was built on complex mountainous terrain with significant fluctuations in Southwest China. The site contains large areas of high fill susceptible to uneven ground deformation from filling material consolidation, dynamic loading from aircraft, and other factors. Thus, monitoring and analyzing the causes and characteristics of postconstruction deformation of high-fill foundations are crucial to the airport's safe operation. In this study, we obtained a total of 149 Sentinel-1A ascending SAR images from March 2017 to March 2022. We estimated the elevation error and corrected the topographic phase to mitigate the impact of large topographic fluctuations on monitoring. Then, we extracted ground subsidence results based on time-series InSAR technology. The results show that deformation mainly occurred in the high-fill areas during the monitoring period, whereas settlement was more pronounced when the fill height was over 30 m. The deformation rate is influenced by the height of the fill, ground reinforcement measures, and dynamic loading of aircraft. Using the Mann-Kendall trend analysis and Pettitt mutation test methods to detect temporal information from time-series points, we found that the time required for the foundation to reach a stable state after construction is not directly related to its residual subsidence. Other factors, such as construction measures also influence it.

Index Terms—DEM error correction, high-fill foundation, Mann-Kendall (MK) trend analysis, Pettitt mutation test, time-series InSAR analysis.

I. INTRODUCTION

KUNMING Changshui International Airport (KCIA) is positioned as China's national gateway hub airport facing Southeast Asia, South Asia, and connecting Europe and

Manuscript received 24 June 2023; revised 25 August 2023 and 4 October 2023; accepted 24 October 2023. Date of publication 30 October 2023; date of current version 23 November 2023. This work was supported in part by the Yunnan Fundamental Research Projects under Grant 202201AU070014 and Grant 202301AT070145, in part by the National Natural Science Foundation of China under Grant 42101450, in part by the Project of the "Yunnan Revitalization Talent Support program," and in part by the Yunnan International Joint Laboratory of China-Laos-Bangladesh-Myanmar Natural Resources Remote Sensing Monitoring. (*Corresponding author: Zhifang Zhao.*)

Mingchun Wen and Xin Zhao are with the Institute of International Rivers and Eco-Security, Yunnan University, Kunming 650500, China (e-mail: wmc@mail.ynu.edu.cn; zhaoxin@mail.ynu.edu.cn).

Mengshi Yang and Zhifang Zhao are with the School of Earth Sciences, Yunnan University, Kunming 650500, China, and also with the Yunnan International Joint Laboratory of China-Laos-Bangladesh-Myanmar Natural Resources Remote Sensing Monitoring, Kunming 650500, China (e-mail: yangms@ynu.edu.cn; zhaozhifang@ynu.edu.cn).

Digital Object Identifier 10.1109/JSTARS.2023.3328321

Asia. The airport was constructed in mountainous areas with large elevation differences. Such construction projects often require a large amount of filling, resulting in the use of local materials and soil-rock mixtures with complex physical and mechanical properties [1]. Previous studies have indicated that the postconstruction deformation of a high-fill foundation is mainly related to the properties of the original foundation, the thickness of the compressed layer, and the height of the filling material. [2]. The main reason for this deformation is the consolidation and creep deformation of the filling, and compaction of the original foundation under the upper filling [3], which usually takes 3–5 years to stabilize [4]. However, previous studies focus on the calculation and monitoring of the deformation during the construction period. These studies have typically employed mechanical theory or deep learning methods to predict the deformation during operation [5], [6]. However, it is difficult to obtain sufficient data to validate the above theories through traditional measurement methods, such as leveling and GNSS. Consequently, the long-term deformation monitoring of high-fill foundations after the construction period is of great significance to understand the settlement process and provide a reference for the prevention and maintenance of airport operations.

The time-series InSAR technology, developed in recent years [7], [8], [9], [10], [11], [12], [13], is known for its low acquisition cost, wide coverage, and long monitoring period. However, it is affected by the decorrelation of long spatial and temporal baselines. To overcome this issue, small baseline subset InSAR (SBAS-InSAR) technology uses shorter spatio-temporal baseline thresholds to form a small baseline set, resulting in better interferograms [14]. This eliminates the spatio-temporal decorrelation problem and topographic errors during conventional interferometric processing. These advanced InSAR methods have been widely used in monitoring studies of regional surface or specific infrastructure deformation, the reliability of which has been verified by many studies [15], [16], [17], [18], [19], [20]. For example, Wang et al. [21] monitored the deformation of high-fill foundations during the construction of Anju airport based on SBAS-InSAR and revealed the mechanism of deformation by numerical simulation methods; Zhang et al. [22] retrieved the time-series result over 2020–2021 of Ankang airport and found that the deformation was mainly caused by

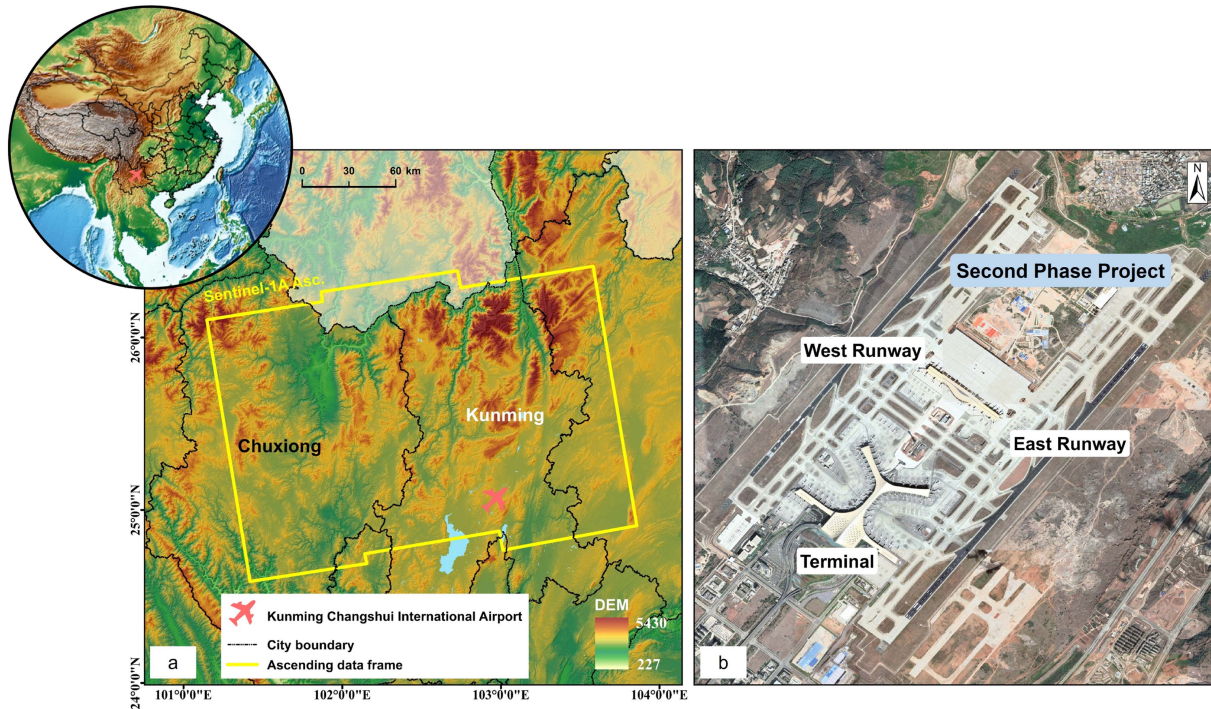


Fig. 1. (a) Study area location and SAR image coverage. (b) 2022 Landsat-8 optical image of KCIA.

consolidation, and the degree of consolidation was affected by the height of the fill and precipitation. It can be seen that these studies covered a short period, the foundation was still in a period of fast consolidation, and further monitoring is therefore required to better understand the process from consolidation to stability of the foundation.

This study presents the time-series InSAR results of KCIA from 2017 to 2022. The results were obtained from ascending images of the Sentinel-1 satellite and cover a five-year period after construction. Analyzing these time-series results, we investigated the correlation between residual deformation postconstruction and fill height. Then, we applied the MK trend analysis and the Pettitt mutation test to exclude any anomalous series and identify the time of impact. Additionally, we observed the impact of various construction factors on foundations.

The rest of this article is organized as follows. In Section II, we introduce the engineering overview of the study area and the data sources. The methodology of retrieving deformation with time-series SAR data and the trend test method of time series are introduced in Section III. The results are presented in Section IV. We analyze the spatio-temporal characteristics of the time-series results and discuss the postconstruction deformation characteristics of the high-fill foundation in combination with the excavation and filling of the airport in Section V. Finally, Section VI concludes this article.

II. STUDY AREA AND DATASET

A. Study Area

The KCIA is located in the northeast of Kunming city, Yunnan province, China, about 24.5 km away from the center of Kunming city, covering an area of about 21 km². It has two runways and two taxiways, which can be divided into the west

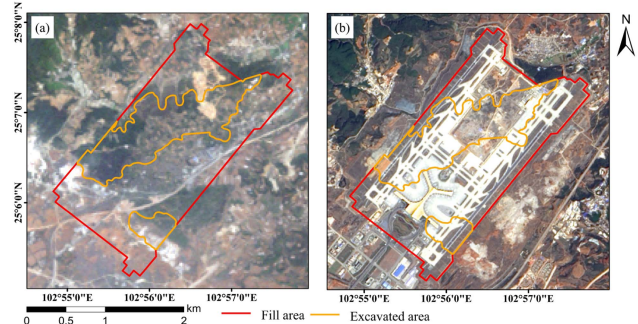


Fig. 2. Optical image before and after the construction of KCIA; the curve line indicates the excavation and filling area. (a) Optical image of Landsat-4 before construction. (b) Optical image of Landsat-7 after completion of construction.

runway area, the east runway area, the terminal building, and the second phase project area [see Fig. 1(b)]. The east runway is 4000 m in length and 60 m in width, whereas the west runway is 4000 m in length and 45 m in width.

The KCIA was built on December 5, 2008, and the main structure of the terminal was completed in 2012 and began operation in the same year. The second phase project started in September 2018, of which the satellite building was built in 2020, and the rest of the project was scheduled to be completed in 2027. The original topography of the airport is dominated by gullies and valleys, with large topographic relief and uneven soil thickness, and the original foundation mainly consists of soft soils such as red clay and secondary red clay [23]. Fig. 2(a) shows the Landsat-4 optical image before the construction of the airport. From the image, there is a northeast-trending mountain through the whole site area. According to the original DEM data, the lowest elevation of the original ground of the east runway is

TABLE I
MAIN PARAMETERS OF THE SAR IMAGE

Parameters	Sentinel-1
Orbit direction	Ascending
Coverage time	March 2017 to March 2022
Number of data	149
Revisit time (day)	12
Wavelength (cm)	5.6
Azimuth/range pixel spacing (m)	14.0/2.3
Central incidence angle (°)	41.8

2063 m, and the lowest elevation of the west runway is 2048 m. To reach the design elevation of 2100 m, the excavation and filling work was carried out in the site area, and the distribution is shown in the middle line of Fig. 2.

B. Dataset

Sentinel-1 is a two-satellite Earth observation system developed by the Copernicus Global Earth Observation Program of the European Space Agency. Its single-satellite re-entry period reaches 12 days, and the spatial baseline can be controlled within 200 m. This study focuses on the settlement of high-fill foundations after construction, where the consolidation of foundations is usually in the vertical direction [19], [22], [24]. The surfaces in the airport were flat, and the objects we observed weren't affected by the geometric distortions depending on the imaging geometry and local topography [25]. Therefore, we utilized the line-of-sight (LOS) velocity results for a single track to retrieve the deformation signals. A total of 149 Sentinel-1 ascending images were acquired from March 2017 to March 2022. The main parameters are shown in Table I.

The ALOS PALSAR 12.5 m resolution digital elevation model covering Yunnan province was also collected for accurate co-registration of SAR images, estimation of terrain phase, and geocoding the InSAR results from Doppler coordinates to the WGS84 coordinate system. The excavation, filling distribution, and engineering geological data of the airport were used in conjunction with the InSAR monitoring results to analyze the spatio-temporal characteristics of the postconstruction deformation.

III. METHODS

The airport site was monitored by time-series InSAR technology. Then, the MK trend analysis and Pettitt mutation test methods were introduced to explore the time-series information that we could combine the time-series results with the collected engineering data, such as excavation and filling information, monitoring points data, and construction measures for comparative analysis, to reveal the spatial distribution and temporal trend. The specific research flowchart is shown in Fig. 3.

A. SBAS-InSAR Processing

The SBAS-InSAR technology is proposed by Berardino et al. [14], which selects interferometric pairs with small spatial and temporal baselines to establish a small subset of baselines. It can effectively alleviate the decorrelation mainly caused by changes in the surface backscatter characteristics over time [25], [26]. The main processing flows in this article are as follows.

1) *Image processing*: First, we cropped and extracted parameters from the collected single-look complex images to obtain information such as incident angle, ephemeris time, orbital attitude vector, etc. Then, the image of 20170723 was used as the master image, and an external DEM was used to accurately co-register to it [2], [27], [28].

2) *Generation of small baseline datasets*: Due to the precise control of Sentinel-1 orbit, the spatial baseline has little effect on interferograms' coherence, and it was observed experimentally that some of the interferometric pairs showed obvious decorrelation after the time baseline was larger than 60 days, so the spatial baseline threshold was set to 150 m, and the time baseline threshold was set to 48 days to obtain high-quality interferometric pairs. A total of 547 interferograms were generated.

3) *Interferometric and unwrapped phase data set*: The master and slave images were interfered with according to the interferogram network. Then, we used the accurate orbit data to remove the phase generated by the flat earth effect. The topographic phase was estimated and removed using ALOS PALSAR 12.5 m DEM. Still, there is a large deviation of this elevation value in the study area due to the excavation and filling. Therefore, there exists a significant phase error caused by topographic errors after the interferometric processing, it could be expressed by the following equation [29]:

$$\Delta\varphi_{\text{top}}(x, r) = \frac{4\pi}{\lambda} \frac{B_{\perp}(t_A, t_B)}{R \sin(\theta)} \Delta h \quad (1)$$

where $B_{\perp}(t_A, t_B)$ is the perpendicular baseline between t_A and t_B , R is the range between the target and the antenna, θ is the look angle, and Δh is the value of the elevation error on each image pixel estimated based on the DEM correct method proposed by Berardino et al. [14] and Fattahi et al. [30]. Through (1), we can calculate the phase error and remove it from the interferogram. The noise phase could be suppressed through multilook filtering and adaptive filtering methods; in this work, the interferograms were multilooked by four pixels in range and one pixel in azimuth, resulting in a spatial resolution of approximately 15 m. Finally, the unwrapped phase dataset is obtained by using the minimum cost flow method.

4) *Retrieval of time-series results*: The retrieval of time-series results in this study was processed with Miami InSAR time-series software in Python (Mintpy) software analysis package [31]. The phase values of any pixel (x, r) in the unwrapped interferograms obtained in the previous step are

$$\begin{aligned} \delta\varphi_i(x, r) = \varphi_B(x, r) - \varphi_A(x, r) \approx \frac{4\pi}{\lambda} [d(t_B, x, r) \\ - d(t_A, x, r)] + \Delta\varphi_{\text{atm}}(x, r) \end{aligned} \quad (2)$$

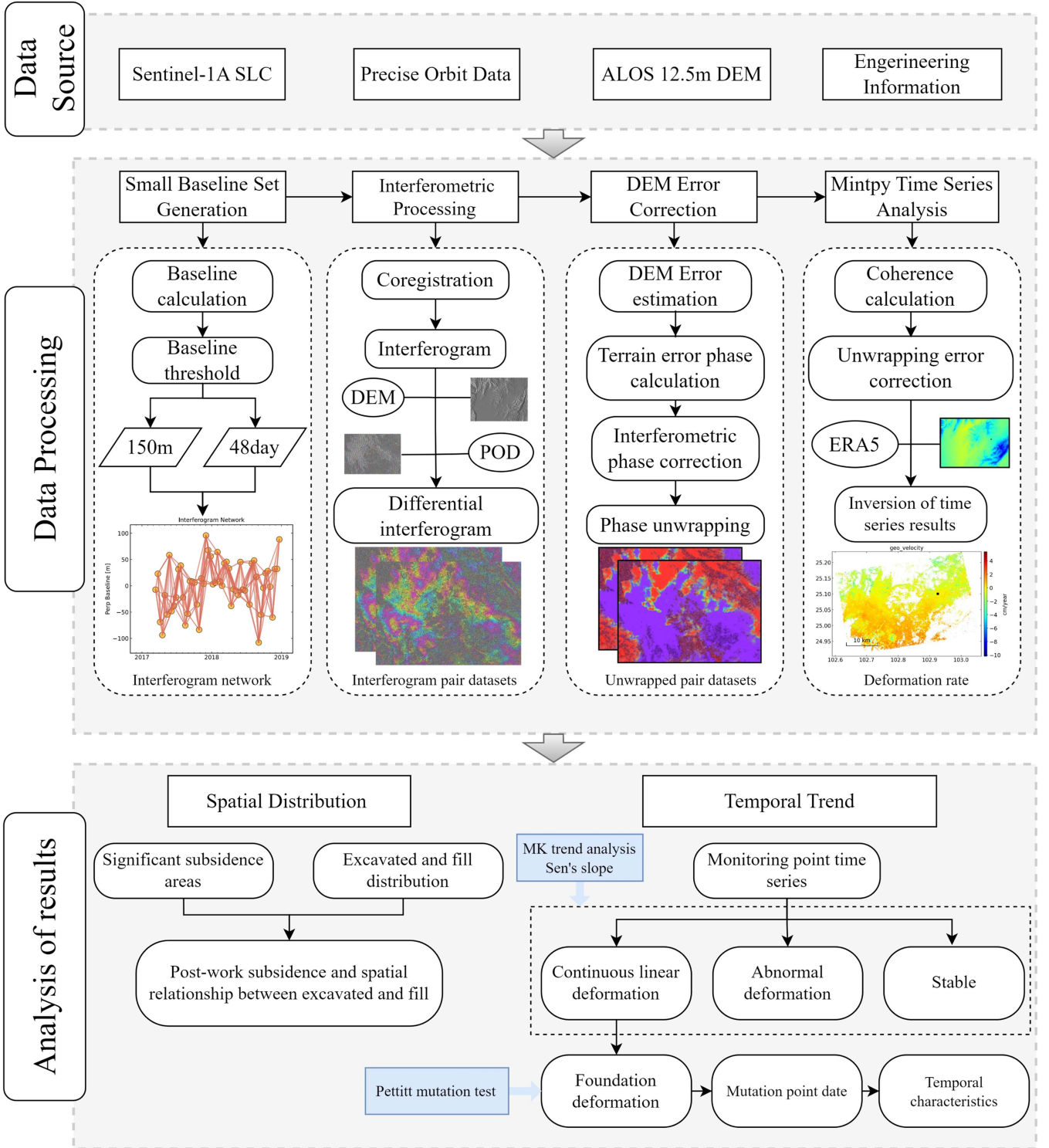


Fig. 3. Flowchart of study.

where $\varphi_B(x, y)$ and $\varphi_A(x, y)$ are the phase at the moments t_B and t_A ; $d(t_B, x, y)$ and $d(t_A, x, y)$ are the cumulative LOS deformation at the moments t_B and t_A , respectively, with respect to the reference moment t_0 ; $\Delta\varphi_{\text{atm}}(x, r)$ represents the atmospheric error and the atmospheric correction using the ERA5 dataset [32]. λ is the radar wavelength.

Assuming that the deformation rate of each image interval is linear [33], the relationship between the deformation rate and the phase can be written as

$$d(t_B, x, r) - d(t_A, x, r) = V_j (t_B - t_A) \quad (3)$$

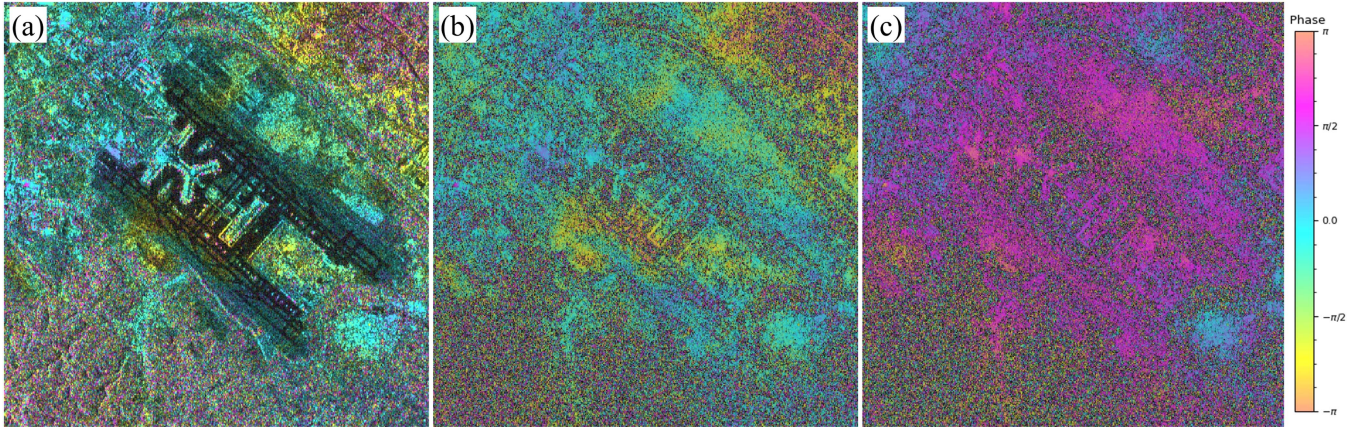


Fig. 4. Comparison of DEM error phase correction. (a) Interferometric phase before correction superimposed on airport intensity image. (b) Interferometric phase before correction. (c) Interferometric phase map after correction.

where V_j denotes the linear deformation rate between t_B and t_A moments, the rate is solved by substituting (3) into (2) to become a least squares (LS) problem. Since the coefficient matrix is a singular matrix, the singular value decomposition method is used to solve it. The accumulated deformation between image intervals is obtained by integrating the linear rate. Then, the root mean square (RMS) and median absolute deviation (MAD) value were calculated for each SAR acquisition; we mark a SAR acquisition as noisy if its RMS value is larger than three times the minimum MAD value [34], which will be discarded in the displacement time series. Finally, the velocity is estimated as the slope of the best-fitting line to the displacement time series.

B. Mann-Kendall Trend Analysis and Pettitt Mutation Test

1) *Mann-Kendall Trend Analysis*: The MK test statistic is a nonparametric statistical method that is aimed to measure whether the variable has a monotonically increasing or decreasing trend in time series [35], [36]. This trend test method had been widely cited in water quality, precipitation, temperature, and other hydrometeorological series, but was rarely used in the series of subsidence. In this study, we mainly used the time-series trend detection method to detect sequences like the type labeled in Fig. 11. The MK test statistic S is calculated as

$$S = \sum_{i=1}^{n-1} \sum_{j=i+1}^n \text{sgn}(x_j - x_i) \quad (4)$$

where n is the number of images, x_i and x_j are the values in time series i and j ($j > i$), respectively, and $\text{sgn}(x_j - x_i)$ is the sign function. The significance of a trend is evaluated using the standardized test statistic Z_S which is computed as

$$Z_S = \begin{cases} S - 1/\sqrt{\text{Var}(S)}, & \text{if } S > 0 \\ 0, & \text{if } S = 0 \\ S + 1/\sqrt{\text{Var}(S)}, & \text{if } S < 0 \end{cases} \quad (5)$$

where $\text{Var}(S)$ is the variance value of S . The positive and negative Z_s values indicate increasing and decreasing trends. This study tests for either an upward or downward trend at the

$\alpha = 0.01$ level of significance ($z_{1-\frac{\alpha}{2}} = 2.576$) H_0 assumes that this time series has no monotonic trend which will be rejected if $|Z_S| > z_{1-\frac{\alpha}{2}}$.

We used the “prewhitening” treatment to eliminate the influence of serial correlation on the MK test. Since the design of the runway allows certain deformation [37], we also use Sen’s slope to evaluate the significance of the trend and set a threshold to consider that the trend within the threshold is also a stable time series [38].

2) *Pettitt Mutation Test*: Pettitt mutation test method is used to identify a single mutation point, which can identify the most reliable point in the time series that causes a significant change in the mean value of the preceding and following series [39], [40]. This method considers the time-series x_1, x_2, \dots, x_r arbitrarily split into two parts x_1, x_2, \dots, x_t and $x_{t+1}, x_{t+2}, \dots, x_r$. If the distribution function of the two component variables is $F_1(x)$ and $F_2(x)$, respectively, and $F_1(x) \neq F_2(x)$, then the mutation point is identified as occurring at time t . The Pettitt test statistic U is calculated as

$$U_{t,r} = \sum_{i=1}^t \sum_{j=i+1}^r \text{sgn}(x_j - x_i) \quad 1 \leq t \leq r. \quad (6)$$

The point τ that satisfies the following equation is recognized as the most probable mutation point.

$$K_\tau = |U_{\tau,T}| = \max |U_{t,T}| \quad (7)$$

the probability of significance of the variable point τ can be obtained by approximating the following equation:

$$p = 2e^{\frac{-6k^2}{T^2+T^3}} \quad (8)$$

at the $\alpha = 0.01$ level of significance H_0 assumes that τ is not a mutation point which will be rejected if $p < \alpha$.

IV. TIME-SERIES INSAR RETRIEVED RESULTS

After estimating the DEM errors, we corrected the phase errors caused by topography from the interferograms. In Fig. 4(a), we present an example of an interferogram generated from

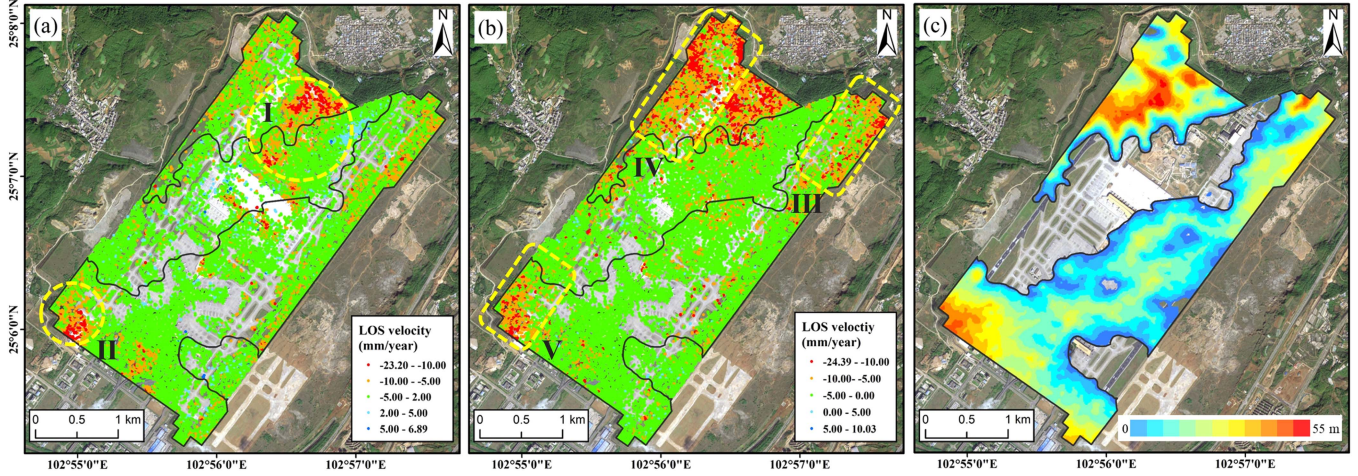


Fig. 5. Deformation rate map for airport monitoring in different time periods compared to fill height distribution. (a) March 2017 to March 2022. (b) March 2017 to January 2019 inversion results. (c) Fill height distribution map.

images acquired on March 28, 2021, and April 9, 2021. In the excavation areas, there were significant phase differences subject to the topographic phase [yellow area in Fig. 4(a) and (b)]. However, the time baseline of this image pair is 12 days, there should be no obvious phase change in the interferogram. After the phase correction, the interferometric phase shown in Fig. 4(c) is more consistent with the deformation situation during the image interval. After correcting the DEM errors, a new interferometric dataset was generated, and then the time-series results were retrieved.

Fig. 5(a) shows the LOS deformation results from March 2017 to March 2022. Since vertical deformation dominates in the surface deformation of high-fill airports [41], we considered negative values of deformation rate to indicate subsidence, whereas positive values represent uplift motions. A total of 41525 coherent points were selected, providing a point density of 3775 per km² of the study area. The results illustrate that the site maintains a stable trend in most areas, with 33 434 points exhibiting a deformation rate within $[-5, 5]$ mm/year, accounting for 80.5%, and 1484 points with a rate < -10 mm/year, accounting for 3.6%. We could observe two areas with significant settlement from the deformation rate map. In area I, which was affected by the construction of the second phase project, the maximum rate reached -19.59 mm/year. In area II, the maximum rate reached -23.2 mm/year, which might have been caused by the sliding of the high-fill slopes.

Considering the settlement characteristics of the high-fill foundation, the process goes from slow consolidation to a stable period. As the deformation rate is estimated as the slope from the displacement time series, a longer monitoring period or the existence of a stable displacement time series leads to some deformation trends being ignored from the rate map. Therefore, we shortened the monitoring period to better detect these deformation trends, and Fig. 5(b) shows the LOS deformation results from March 2017 to January 2019. A total of 48 052 coherent points were obtained, with 37 734 points exhibiting a deformation rate within $[-5, 5]$ mm/year, accounting for 78.6%,

and 3815 points with a rate > 10 mm/year, accounting for 8%. By comparing the rate results of two time periods, we found that the deformation was still evident in area I, which coincides with the construction period of the second phase project. Moreover, in the high-fill areas with filling height > 20 m, as shown in Fig. 5(c), we could see evident subsidence which was not detected before. Then, we divided the high-fill areas into three areas, and the spatio-temporal characteristics of the deformation in these areas will be analyzed in the next section.

V. DISCUSSION

This section discusses the factors that affect deformation in the KCIA's foundation. We analyzed the relationship between abnormal areas and these factors using InSAR results. Based on the MK test, we identified the time-series points that reflect the consolidation process of the foundation. The spatio-temporal characteristics of postconstruction deformation were analyzed as follows.

A. Characteristics of High-fill Foundation Construction in KCIA

For KCIA's foundations, we divided them into two types based on excavation and filling conditions: original foundations and high-fill foundations. The original foundations mainly consisted of original red clay, which also explained that in the excavated areas, as shown in Fig. 5(a) and (b), which were subjected to runway and dynamic loads from aircraft. During the construction period, this type of foundation had been stabilized by compacting measures.

The high-fill foundation consists of two parts, as shown in Fig. 6(a), the lower original red clay foundation and the upper coarse-grained filling body. Deformation usually occurs because of the settling of the upper fill and the compaction deformation of the underlying foundation caused by the dynamic load. Among them, the deformation caused by the original red clay gradually decreases during filling. Thus, the postconstruction deformation

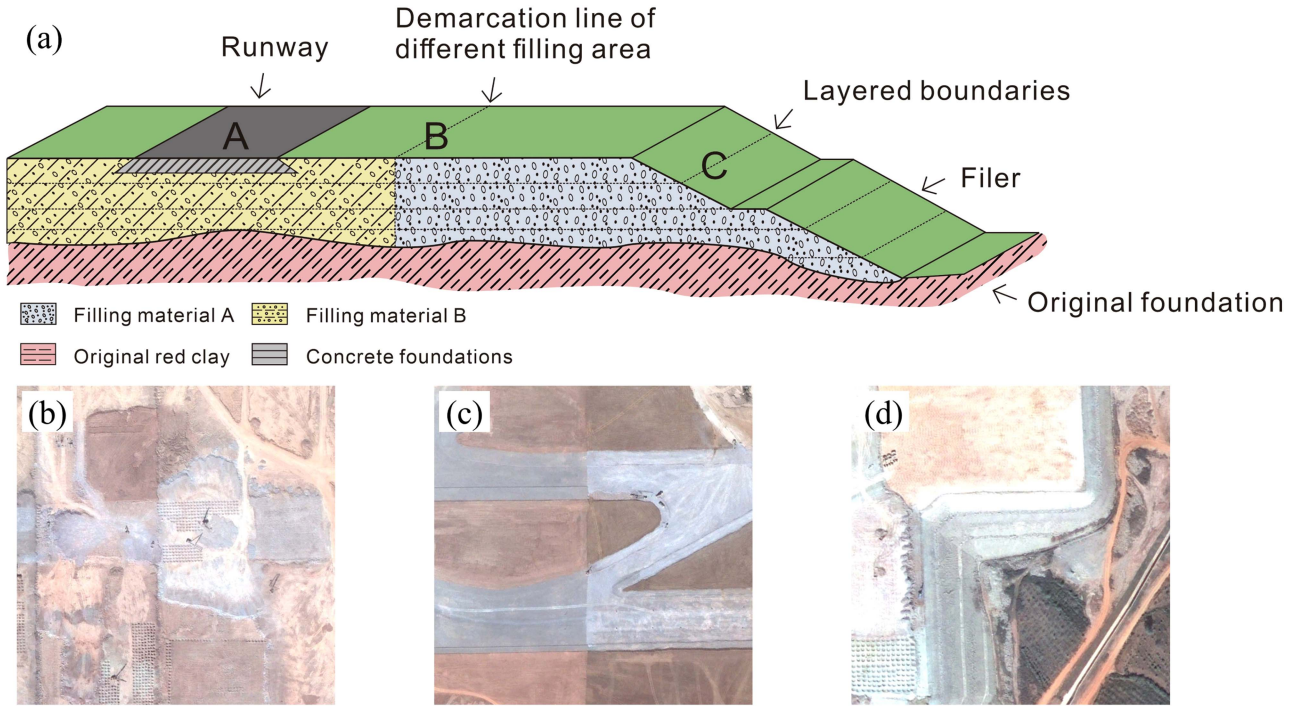


Fig. 6. Diagram of high-fill construction. (a) Composition of high-fill foundation. (b) Area A, construction of concrete pad under runway surface. (c) Area B, significant partitioning due to filling with different fill materials. (d) Area C, significant partitioning at side slopes due to layered filling.

mainly comes from the filler. Previous research indicated that the postconstruction deformation is positively correlated with the height of filler, and proposed the empirical estimation equation as follows: [42]:

$$s = \frac{h^2}{3\sqrt{E^2}} \quad (9)$$

where s is the final settlement of the high fill, h is the height of the filler, and E is the deformation modulus of the fill material. However, the deformation results show that the deformation is also influenced by the actual construction situation. For example, the runway is a crucial facility for airport operation and must withstand dynamic loading from aircraft taking off and taxiing. As a result, the fill material under the runway must be more reliable. Fig. 6(b) shows the construction of the concrete pad beneath the runway surface. The fill volume of KCIA reaches 100 million m^3 , the cost of transporting the fill material from off-site is too high, and the fill material is usually obtained from the vicinity of the fill area, resulting in different fill materials for each fill area. Figs. 6(c) and 7 show the boundary between the different filling areas, which were divided into ten areas from T1–T10. A high-fill foundation usually adopts a layered filling method of 4–5 m, the gaps between the fill layers that are difficult to be compacted, leading to more deformation. Fig. 6(d) shows the layered filling of a high-filling body. In addition, there are other factors that affect the postconstruction deformation. By collecting data from the site monitoring points (see Fig. 7), the specific information is shown in Table II.

The deformation affected by the above factors will be further analyzed in the next section.

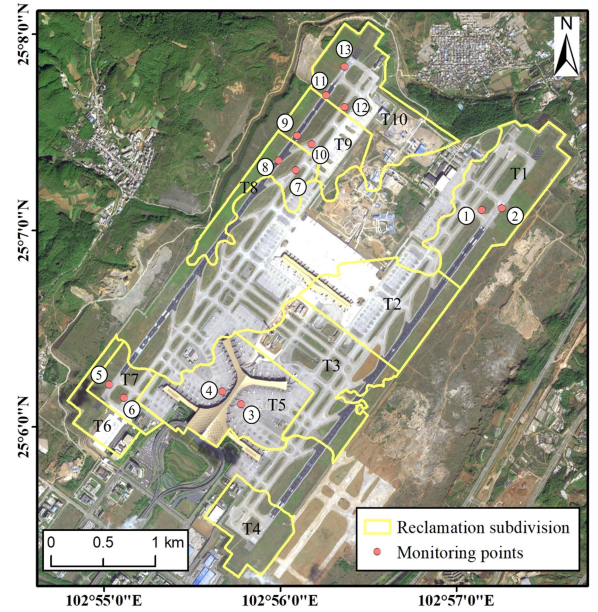


Fig. 7. Airport filling areas and monitoring points distribution map.

B. Deformation Pattern in High-Fill Areas

Residual settlement is an important indicator to reflect the consolidation of the foundation, which could be estimated by the deformation rate. We created three profile lines in high-fill areas, obtained the elevation on the profile, and extracted the deformation rate in the 15 m area along the line that matched

TABLE II
THICKNESS AND TREATMENT OF THE ORIGINAL FOUNDATION AND FILL AT DIFFERENT MONITORING POINTS

No.	Original foundation thickness (m)	Filler thickness (m)	Original foundation treatment	Filler treatment
1	10.0	22.0	Dynamic consolidation	Vibration rolling
2	12.1	24.5	Dynamic consolidation	Vibration rolling
3	7.5	27.0	Dynamic consolidation	Dynamic consolidation
4	4.0	28.5	Dynamic consolidation	Rolling, consolidation
5	3.5	24.5	None	Impact, consolidation
6	6.3	36.5	Dynamic consolidation	Dynamic consolidation
7	14.0	38.0	Stone Column	Impact
8	15.4	42.5	Stone Column	Impact
9	18.0	35.0	Dynamic consolidation	Impact
10	17.0	39.0	Stone Column	Impact
11	11.4	43.0	None	Dynamic consolidation
12	6.6	50.0	None	Dynamic consolidation
13	16.0	21.5	Dynamic consolidation	Impact, consolidation

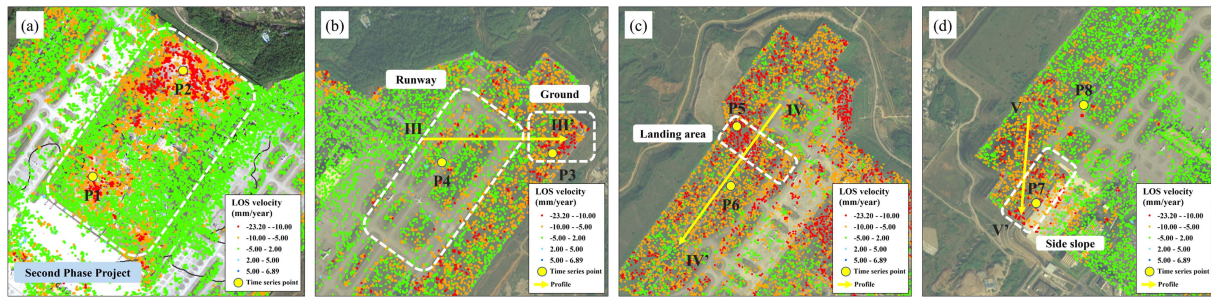


Fig. 8. Local enlargement of high-fill areas. (a) Local enlargement of area I. (b) Local enlargement of area III. (c) Local enlargement of area IV. (d) Local enlargement of area V.

the spatial resolution (see Fig. 8). The Y -coordinate in Fig. 9 was the average of all velocities in the $15\text{ m} \times 15\text{ m}$ cell, in which the error bar was the standard deviation of the velocities.

Profile line III-III' extended from the runway to the top of high side slope. Fig. 9(a) and (b) shows a comparison and correlation between velocity and fill depth. The range of 0–600 m is mainly located on the taxiway, where the fill is stable during the monitoring period due to its small depth and concrete foundation reinforcement on the surface. The range of 600–800 m is bare ground, and the fill depth in this section has a better positive correlation with velocity. Profile line IV-IV' is located on the north end of the west runway. Fig. 9(c) shows that the section of 200–400 m is located at the aircraft landing point, which is mainly subjected to dynamic loading of the aircraft, whereas this area is adjacent to monitoring point 11 in Table II, and the height of fill in the vicinity of this point reaches 40 m. The original foundation was not reinforced, resulting in an obvious settlement phenomenon. The rest of the section on profile line IV-IV' is less affected by the consolidation of the foundation. As shown in Fig. 9(d), the correlation coefficient is 0.435 due to the runway reinforcement measures. Profile line V-V' is located on the south end of the west runway. Fig. 9(e) shows that the section from about 0–350m is bare ground, and in this section, there has better correlation between velocity and fill depth. The

range of 350–500 m section is the runway area, which was influenced by the foundation reinforcement, despite the filling volume was large the velocity returned to a stable level. The 500–600 m section is the side slope at the south end, and the filling height of this section reaches 50 m. It may be affected by abnormal deformation phenomenon caused by unstable sideslip of high side slope [43], [44]. This will be further analyzed by time-series results in the next section.

Based on the comparison above, a positive correlation between residual settlement and fill depth in bare ground has been observed. However, this relationship may be affected by reinforcement measures and dynamic loading. Fig. 10 shows the classification of all the obtained deformation points into four categories, namely filling height $<0\text{ m}$, within 0–30 m, $>30\text{ m}$, and $>40\text{ m}$. It can be seen that when the filling height is less than 30, the obtained time-series points are basically stable, and the station ratios are 91% and 77.4%, respectively. When the filling height is $>30\text{ m}$, there are 71% and 75% of the time-series points to detect obvious subsidence. This might be caused by layering of fill material, there are loose areas of gaps between the layers, and the loose areas increase when the fill height is larger, resulting in more residual settlement after work. This further explains the effect of fill height on the residual deformation in areas without special reinforcement measures.

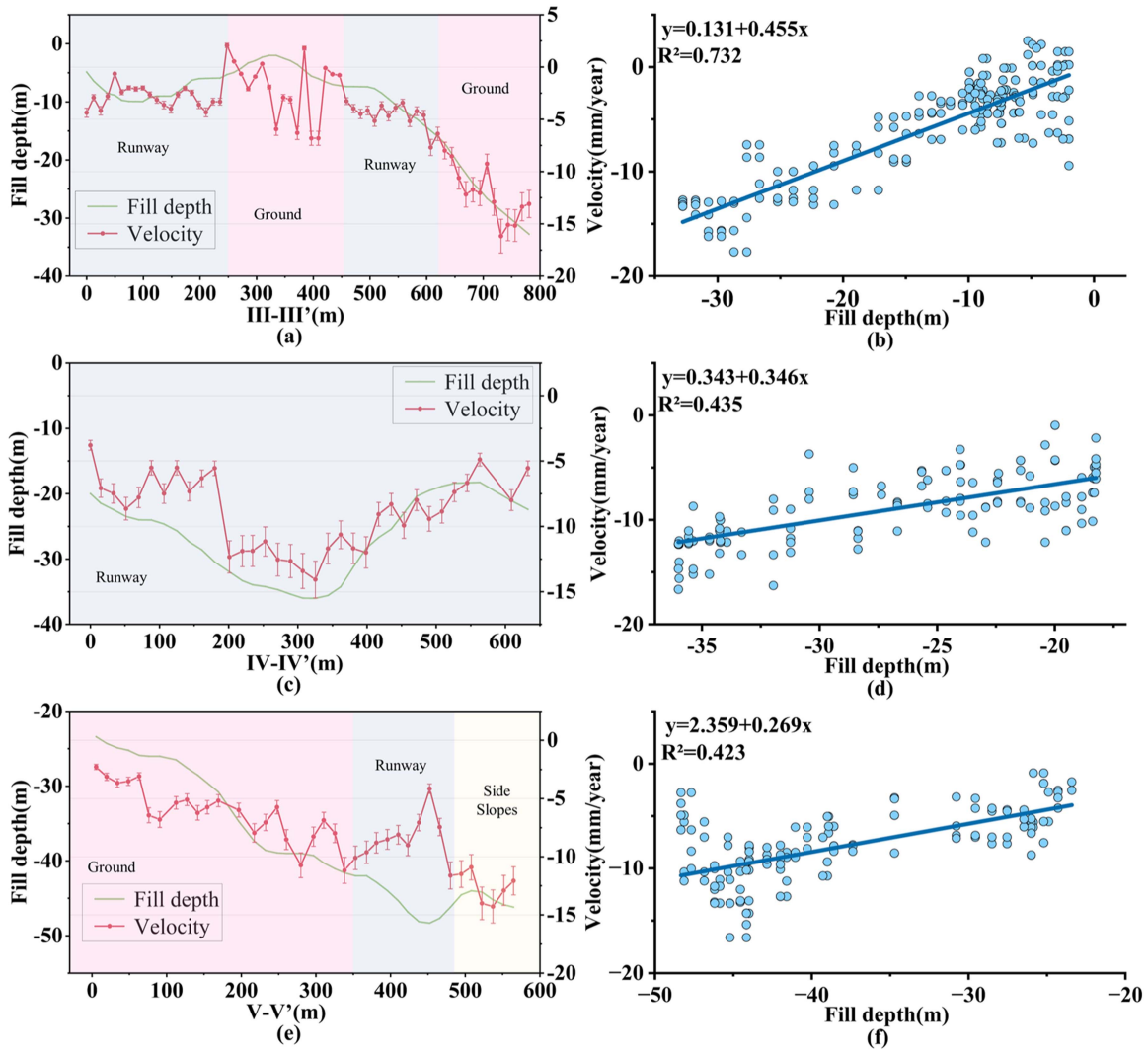


Fig. 9. Deformation area rate profiles and correlation plot.

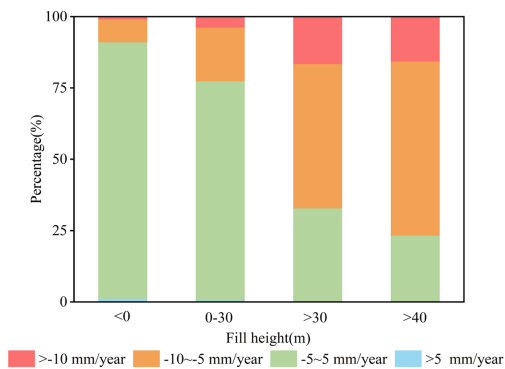


Fig. 10. Time-series point rate distribution under different filling heights.

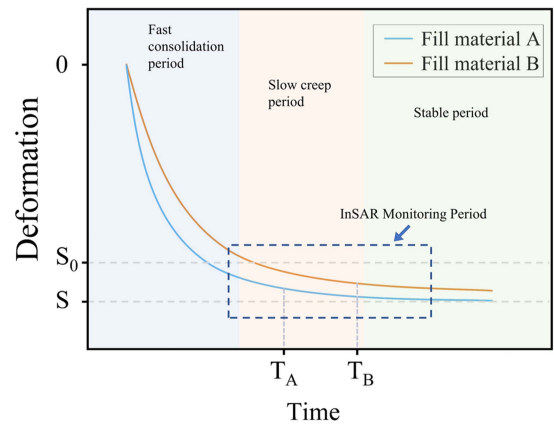


Fig. 11. Schematic diagram of settlement curve for different fills.

C. Spatio-Temporal Characteristics of Foundation Deformation at KCIA

The settlement process of a high-fill foundation can be divided into three stages, as shown in Fig. 11. The first stage is

characterized by the rapid settlement of the foundation due to its own gravity and compacting measures. The second stage is marked by the slow creep, and the third stage is when the

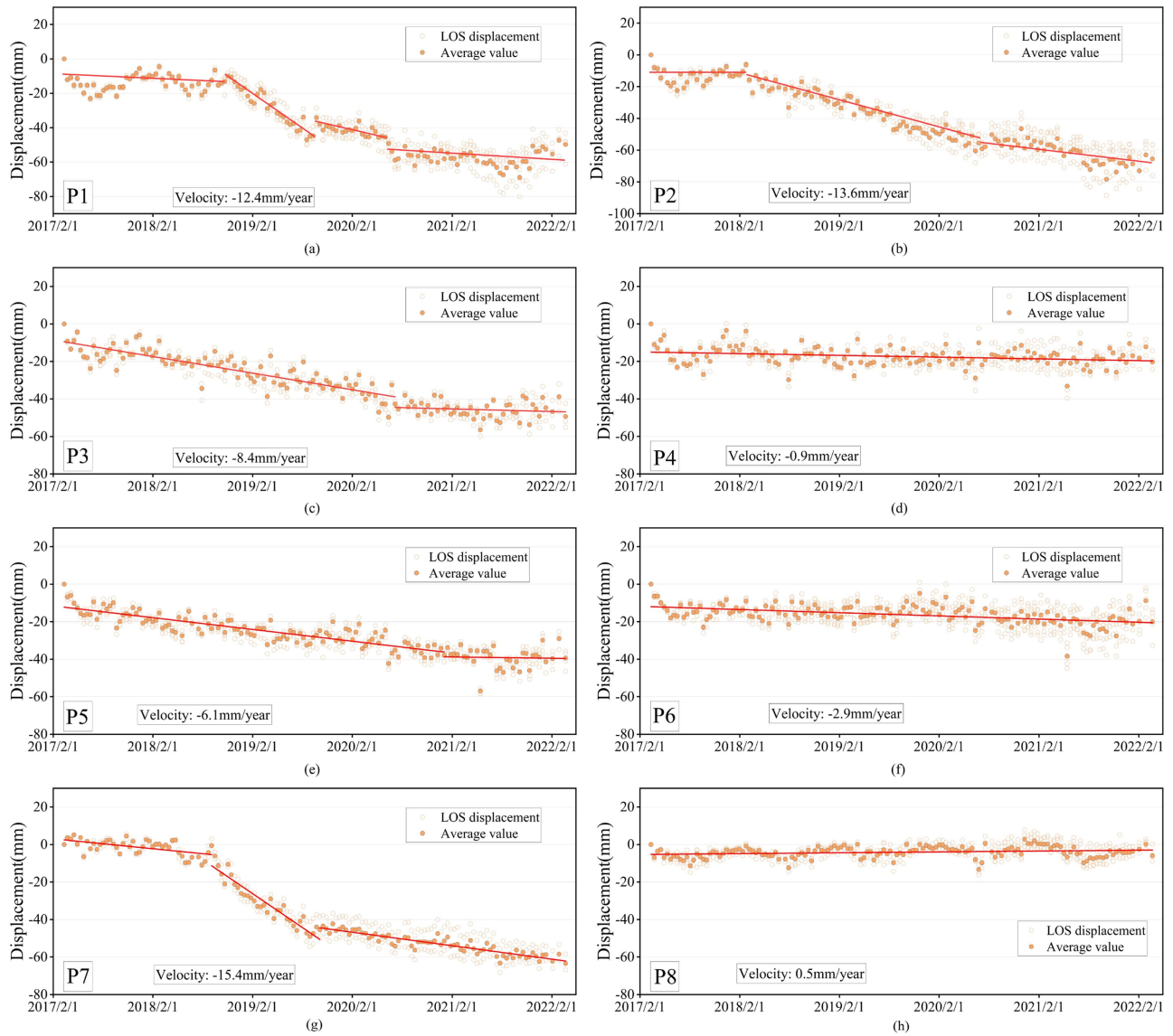


Fig. 12. Time-series displacements of eight typical monitoring points in Fig. 8.

foundation becomes stable. Fig. 11 shows the residual settlement curves for different fill materials. Here, S represents the total settlement of the fill, whereas S_0 represents the settlement that occurs during the fast consolidation period. The residual settlement after construction is calculated by subtracting S_0 from S and typically takes 3–5 years to stabilize. T_A and T_B represent the time required for different types of fill material to enter the stable period. However, the time required to reach this stage is complex due to the difference in the mechanical properties and other factors.

Through the monitoring for different periods, we detected different deformation areas between the two results (see Fig. 5). In the monitoring results from 2017–2019, there is a significant settlement in high-fill areas, whereas, in results from 2017–2022, these areas were stabilized which coincides with the deformation curve above. It can be confirmed by the time-series displacements of the selected points. Fig. 12 shows the time-series results

of selected points P1–P8, respectively. P1 and P2 are located in the second phase area. They show several stages of displacement changes due to the construction of the second phase project. P4, P6, and P8 are located on the runway. It could be seen that the runway has basically been in a stable state after operation for 5 years. P3 and P5 are located on bare ground and reached the stable state successively during the monitoring period, which is consistent with the part marked with a dashed line in Fig. 11. As seen in the time-series result at P7, there is a significant acceleration of the deformation rate in January 2019, which continues for a year before that rate moderates again. We consider that this kind of time series with abrupt changes is inconsistent with the consolidation curve of the foundation. The location of this point on the side slope also confirms our deduction. The time series of P3 and P5 show that we can detect the time point T from the results, but to analyze the temporal characteristics of the deformation. We used the MK trend analysis method to identify

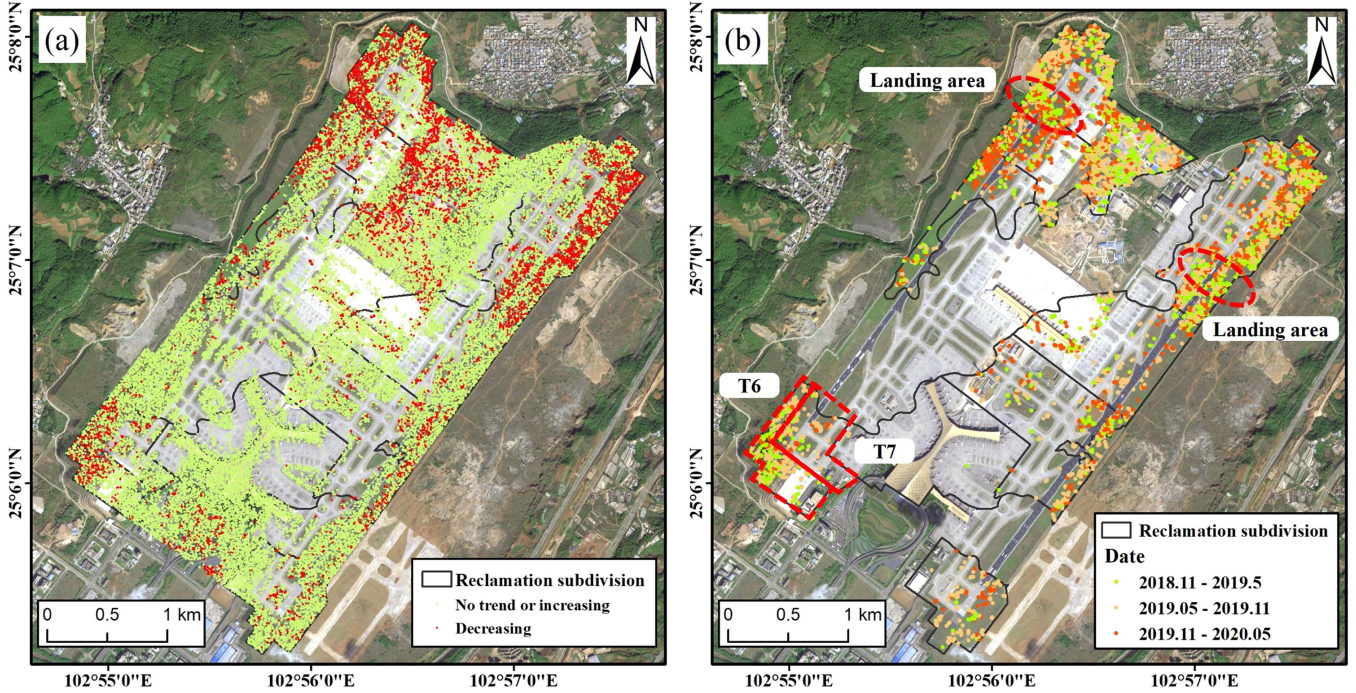


Fig. 13. Trend test and mutation point detection results. (a) MK trend analysis results. (b) Pettitt mutation test results.

TABLE III
TREND TEST AND MUTATION POINT DETECTION RESULTS IN SELECTED POINTS

No.	Trend	Sen's slope	Mutation period
P1	No trend	-0.395	—
P2	No trend	-0.550	—
P3	Decreasing	-0.295	2019.07
P4	No trend	0.027	—
P5	Decreasing	-0.220	2020.02
P6	No trend	-0.013	—
P7	No trend	-0.553	—
P8	Increasing	0.050	—

the time series which can depict the consolidation process of the foundation, and through the Pettitt mutation point test to find the time point T [2]. We first examined the selected points, and the results are shown in Table III.

The MK test detected the decreasing trend effectively, such as points P3 and P5. No trends were detected from the time series for stable time series such as P4 and P6. Although a trend can be detected from the time series of P8, combined with Sen's slope value, the series with the absolute value of Sen's slope value less than 0.1 was considered as no trend. Besides, this method can define the time series with abnormal variation, such as P1, P2, and P7, as no trend. Since the Pettitt method is capable of identifying a single mutation point from a time series, we selected series with a single trend for testing, such as P3 and P5, to obtain a reliable mutation point. The mutation in the time

series of P3 was detected to occur near July 2019 and the P5 occurred near February 2020. This indicates that the foundation at P3 entered the stable period earlier than P5, which is consistent with what is observed in Fig. 12.

Classification of all points by the above method, the results are shown in Fig. 13(a). The green color indicates no trend is detected, which would be excluded before detecting the mutation point. Then, to obtain the time-series points which reflect the consolidation process of the foundation. We excluded the points within the excavation areas. The results of mutation points are shown in Fig. 13(b). We can see that the significant deformation at the fill areas is retained, and the points of abnormal deformation affected by construction and sliding are removed. Besides, we can see that the foundation enters a stable period gradually from November 2018 to May 2020. The earliest time to enter the stable period is in December 2018. After March 2020, most time-series points enter the stable period.

In area T1, we find the foundations away from the runway, enter stable mainly in the period from May 2019 to November 2019 under the effect of consolidation, whereas the foundations along the runway are subject to dynamic loading and will enter stable earlier. Although the fill height in T6 is larger than T7, the foundation in the T6 area enters stable earlier, which may be affected by the construction measures and fill materials. In the areas of T8 and T9, we can see that the time required for consolidation is longer due to the higher fill height. In area T10, the area of foundation away from the runway in which fill height is lower therefore it enters stable earlier. However, in the vicinity of monitoring point 11, which is near the landing point of the aircraft, although the height and the deformation rate are higher here (see Fig. 5), the time required for its consolidation under

the dynamic load is shorter. For the rest of the fill areas, which were excluded because no trend was detected from the time series, we consider that these areas are in a stable period before the monitoring or at the beginning of the monitoring. For time series with abrupt changes at the beginning of monitoring, the trend in this part cannot be detected due to the lack of sufficient time sample values [45], [46], limited by the MK test method. However, with the above results, we can analyze the spatio-temporal characteristics of postconstruction deformation and the influencing factors on it.

VI. CONCLUSION

In this study, the time-series InSAR technology is used to monitor the airport surface after the terrain error phase is corrected to solve the problem that the commonly obtained DEM has a large elevation phase error in the high-fill area. We also introduce the MK test and Pettitt mutation test methods to classify the time-series displacements. This allows us to identify the series that coincide with the foundation consolidation patterns and detect the point that enters the stable period. The results show that the following statements hold.

- 1) After KCIA operation for 5 years, the high-fill areas tend to have obvious deformation, and the maximum deformation rate reaches -24.32 mm/year. Until March 2022, the foundations of the areas mentioned above are stabilized.
- 2) The deformation rate of the high-fill foundation has a certain correlation with the height of the filling body. When the filling height is higher than 30 m, it is easy to occur subsidence phenomenon after construction. However, this phenomenon can be reduced by reinforcing the foundations in crucial areas such as terminals and runways.
- 3) From the time-series results, we can find that the residual deformation after construction is not directly related to the time required for consolidation, which is mainly influenced by the height and material of the fill, but it is also affected by various factors, such as the dynamic load of the aircraft, and the foundation treatment measures and the construction measures.

ACKNOWLEDGMENT

The authors would like to thank the anonymous reviewers and the editors for their valuable comments and suggestions that improved the manuscript.

REFERENCES

- [1] T. Chen, *Study on the Characters of Deformation and Stability of High-Fill Airport Embankment in Mountainous Areas*. Zhengzhou, China: Zhengzhou Univ. Press, 2010.
- [2] A. Kulshrestha, L. Chang, and A. Stein, "Use of LSTM for sinkhole-related anomaly detection and classification of InSAR deformation time series," *IEEE J. Sel. Top. Appl. Earth Observ. Remote Sens.*, vol. 15, pp. 4559–4570, 2022, doi: [10.1109/JSTARS.2022.3180994](https://doi.org/10.1109/JSTARS.2022.3180994).
- [3] G. Cao, *Study on Post-Construction Settlement of High Fill Foundation in Mountainous Airport*. Beijing, China: Tsinghua Univ. Press, 2012.
- [4] Y.-H. Liang, W.-H. Shui, and S.-F. Lu, "Field practice and ground settlement behaviors of a land creation case in loess area of China," *Bull. Eng. Geol. Environ.*, vol. 81, no. 11, Nov. 2022, Art. no. 462, doi: [10.1007/s10064-022-02964-w](https://doi.org/10.1007/s10064-022-02964-w).
- [5] P.-C. Wu, W.-Q. Feng, and J.-H. Yin, "Numerical study of creep effects on settlements and load transfer mechanisms of soft soil improved by deep cement mixed soil columns under embankment load," *Geotextiles Geomembranes*, vol. 48, no. 3, pp. 331–348, Jun. 2020, doi: [10.1016/j.geotexmem.2019.12.005](https://doi.org/10.1016/j.geotexmem.2019.12.005).
- [6] Y. Jie, Y. Wei, D. Wang, and Y. Wei, "Numerical study on settlement of high-fill airports in collapsible loess geomaterials: A case study of Liliang airport in Shanxi province, China," *J. Central South Univ.*, vol. 28, no. 3, pp. 939–953, Mar. 2021, doi: [10.1007/s11771-021-4655-4](https://doi.org/10.1007/s11771-021-4655-4).
- [7] D. Massonnet et al., "The displacement field of the Landers earthquake mapped by radar interferometry," *Nature*, vol. 364, no. 6433, pp. 138–142, Jul. 1993, doi: [10.1038/364138a0](https://doi.org/10.1038/364138a0).
- [8] A. Hooper, "A multi-temporal InSAR method incorporating both persistent scatterer and small baseline approaches," *Geophys. Res. Lett.*, vol. 35, no. 16, Aug. 2008, Art. no. L16302, doi: [10.1029/2008GL034654](https://doi.org/10.1029/2008GL034654).
- [9] A. Ferretti, A. Fumagalli, F. Novali, C. Prati, F. Rocca, and A. Rucci, "A new algorithm for processing interferometric data-stacks: SqueeSAR," *IEEE Trans. Geosci. Remote Sens.*, vol. 49, no. 9, pp. 3460–3470, Sep. 2011, doi: [10.1109/TGRS.2011.2124465](https://doi.org/10.1109/TGRS.2011.2124465).
- [10] A. Ferretti, C. Prati, and F. Rocca, "Permanent scatterers in SAR interferometry," *IEEE Trans. Geosci. Remote Sens.*, vol. 39, no. 1, pp. 8–20, Jan. 2001, doi: [10.1109/36.898661](https://doi.org/10.1109/36.898661).
- [11] R. Bürgmann, P. A. Rosen, and E. J. Fielding, "Synthetic aperture radar interferometry to measure earth's surface topography and its deformation," *Annu. Rev. Earth Planet. Sci.*, vol. 28, no. 1, pp. 169–209, May 2000, doi: [10.1146/annurev.earth.28.1.169](https://doi.org/10.1146/annurev.earth.28.1.169).
- [12] P. A. Rosen et al., "Synthetic aperture radar interferometry," *Proc. IEEE*, vol. 88, no. 3, pp. 333–382, Mar. 2000, doi: [10.1109/5.838084](https://doi.org/10.1109/5.838084).
- [13] X. Shi, L. Zhang, Y. Zhong, L. Zhang, and M. Liao, "Detection and characterization of active slope deformations with sentinel-1 InSAR analyses in the southwest area of Shanxi, China," *Remote Sens.*, vol. 12, no. 3, Jan. 2020, Art. no. 392, doi: [10.3390/rs12030392](https://doi.org/10.3390/rs12030392).
- [14] P. Berardino, G. Fornaro, R. Lanari, and E. Sansosti, "A new algorithm for surface deformation monitoring based on small baseline differential SAR interferograms," *IEEE Trans. Geosci. Remote Sens.*, vol. 40, no. 11, pp. 2375–2383, Nov. 2002, doi: [10.1109/TGRS.2002.803792](https://doi.org/10.1109/TGRS.2002.803792).
- [15] D. Perissin, Z. Wang, and H. Lin, "Shanghai subway tunnels and highways monitoring through cosmo-SkyMed persistent scatterers," *ISPRS J. Photogramm. Remote Sens.*, vol. 73, pp. 58–67, Sep. 2012, doi: [10.1016/j.isprsjprs.2012.07.002](https://doi.org/10.1016/j.isprsjprs.2012.07.002).
- [16] Z. S. Demissie and G. Rimmington, "Surface displacements mechanism of the Dobi Graben from ASAR time-series analysis of InSAR: Implications for the tectonic setting in the central afar depression, Ethiopia," *Remote Sens.*, vol. 14, no. 8, Apr. 2022, Art. no. 1845, doi: [10.3390/rs14081845](https://doi.org/10.3390/rs14081845).
- [17] S. Wu, Z. Yang, X. Ding, B. Zhang, L. Zhang, and Z. Lu, "Two decades of settlement of Hong Kong International Airport measured with multi-temporal InSAR," *Remote Sens. Environ.*, vol. 248, Oct. 2020, Art. no. 111976, doi: [10.1016/j.rse.2020.111976](https://doi.org/10.1016/j.rse.2020.111976).
- [18] M. Yang, T. Yang, L. Zhang, J. Lin, X. Qin, and M. Liao, "Spatio-temporal characterization of a reclamation settlement in the Shanghai coastal area with time series analyses of X-, C-, and L-band SAR datasets," *Remote Sens.*, vol. 10, no. 2, Feb. 2018, Art. no. 329, doi: [10.3390/rs10020329](https://doi.org/10.3390/rs10020329).
- [19] Z. Zhou, X. Yao, K. Ren, and H. Liu, "Formation mechanism of ground fissure at Beijing capital international airport revealed by high-resolution InSAR and numerical modelling," *Eng. Geol.*, vol. 306, Sep. 2022, Art. no. 106775, doi: [10.1016/j.enggeo.2022.106775](https://doi.org/10.1016/j.enggeo.2022.106775).
- [20] X. Qin et al., "A structure knowledge-synthetic aperture radar interferometry integration method for high-precision deformation monitoring and risk identification of sea-crossing bridges," *Int. J. Appl. Earth Observation Geoinf.*, vol. 103, Dec. 2021, Art. no. 102476, doi: [10.1016/j.jag.2021.102476](https://doi.org/10.1016/j.jag.2021.102476).
- [21] T. Wang et al., "Subsidence monitoring and mechanism analysis of Anju airport in Suining based on InSAR and numerical simulation," *Remote Sens.*, vol. 14, no. 15, Aug. 2022, Art. no. 3759, doi: [10.3390/rs14153759](https://doi.org/10.3390/rs14153759).
- [22] S. Zhang et al., "Surface deformation of expansive soil at Ankang airport, China, revealed by InSAR observations," *Remote Sens.*, vol. 14, no. 9, Jan. 2022, Art. no. 9, doi: [10.3390/rs14092217](https://doi.org/10.3390/rs14092217).
- [23] X. Guo, *Research of the Karst Development Environment and Law from Changshui Airport to Xiaoshao in Kunming*. Kunming, China: Kunming Univ. Sci. Technol. Press, 2021.
- [24] G. Zhuo et al., "Evaluating potential ground subsidence geo-hazard of Xiamen Xiang'an new airport on reclaimed land by SAR interferometry," *Sustainability*, vol. 12, no. 17, Aug. 2020, Art. no. 6991, doi: [10.3390/su12176991](https://doi.org/10.3390/su12176991).

- [25] R. F. Hanssen, *Radar Interferometry: Data Interpretation and Error Analysis*, vol. 2. Dordrecht, The Netherlands: Springer, 2001, doi: [10.1007/0-306-47633-9](https://doi.org/10.1007/0-306-47633-9).
- [26] H. A. Zebker and J. Villasenor, "Decorrelation in interferometric radar echoes," *IEEE Trans. Geosci. Remote Sens.*, vol. 30, no. 5, pp. 950–959, Sep. 1992, doi: [10.1109/36.175330](https://doi.org/10.1109/36.175330).
- [27] N. Yagüe-Martínez et al., "Interferometric processing of Sentinel-1 TOPS data," *IEEE Trans. Geosci. Remote Sens.*, vol. 54, no. 4, pp. 2220–2234, Apr. 2016, doi: [10.1109/TGRS.2015.2497902](https://doi.org/10.1109/TGRS.2015.2497902).
- [28] Y. Qin, D. Perissin, and J. Bai, "Investigations on the coregistration of Sentinel-1 TOPS with the conventional cross-correlation technique," *Remote Sens.*, vol. 10, no. 9, Sep. 2018, Art. no. 1405, doi: [10.3390/rs10091405](https://doi.org/10.3390/rs10091405).
- [29] D. Massonnet and K. L. Feigl, "Radar interferometry and its application to changes in the earth's surface," *Rev. Geophys.*, vol. 36, no. 4, pp. 441–500, Nov. 1998, doi: [10.1029/97RG03139](https://doi.org/10.1029/97RG03139).
- [30] H. Fattahi and F. Amelung, "DEM error correction in InSAR time series," *IEEE Trans. Geosci. Remote Sens.*, vol. 51, no. 7, pp. 4249–4259, Jun. 2013, doi: [10.1109/TGRS.2012.2227761](https://doi.org/10.1109/TGRS.2012.2227761).
- [31] Z. Yunjun, H. Fattahi, and F. Amelung, "Small baseline InSAR time series analysis: Unwrapping error correction and noise reduction," *Comput. Geosci.*, vol. 133, Dec. 2019, Art. no. 104331, doi: [10.1016/j.cageo.2019.104331](https://doi.org/10.1016/j.cageo.2019.104331).
- [32] Z. Hu and J. J. Mallorquí, "An accurate method to correct atmospheric phase delay for InSAR with the ERA5 global atmospheric model," *Remote Sens.*, vol. 11, no. 17, Aug. 2019, Art. no. 1969, doi: [10.3390/rs11171969](https://doi.org/10.3390/rs11171969).
- [33] T. R. Lauknes, H. A. Zebker, and Y. Larsen, "InSAR deformation time series using an L_1 -norm small-baseline approach," *IEEE Trans. Geosci. Remote Sens.*, vol. 49, no. 1, pp. 536–546, Jan. 2011, doi: [10.1109/TGRS.2010.2051951](https://doi.org/10.1109/TGRS.2010.2051951).
- [34] P. J. Rousseeuw and M. Hubert, "Robust statistics for outlier detection," *WIREs Data Mining Knowl. Discov.*, vol. 1, no. 1, pp. 73–79, Jan. 2011, doi: [10.1002/widm.2](https://doi.org/10.1002/widm.2).
- [35] H. B. Mann, "Nonparametric tests against trend," *Econometrica*, vol. 13, no. 3, pp. 245–259, 1945, doi: [10.2307/1907187](https://doi.org/10.2307/1907187).
- [36] M. G. Kendall, *Rank Correlation Methods*. Oxford, U.K.: Griffin, 1948.
- [37] S. Yue and C. Y. Wang, "Applicability of prewhitening to eliminate the influence of serial correlation on the Mann-Kendall test: Technical note," *Water Resour. Res.*, vol. 38, no. 6, pp. 4-1–4-7, Jun. 2002, doi: [10.1029/2001WR000861](https://doi.org/10.1029/2001WR000861).
- [38] P. K. Sen, "Estimates of the regression coefficient based on Kendall's tau," *J. Amer. Stat. Assoc.*, vol. 63, no. 324, pp. 1379–1389, Dec. 1968, doi: [10.1080/01621459.1968.10480934](https://doi.org/10.1080/01621459.1968.10480934).
- [39] A. N. Pettitt, "A non-parametric approach to the change-point problem," *J. Roy. Stat. Soc., Ser. C*, vol. 28, no. 2, pp. 126–135, 1979, doi: [10.2307/2346729](https://doi.org/10.2307/2346729).
- [40] D. Rybski and J. Neumann, "A review on the Pettitt test pettitt-test," in *Extremis: Disruptive Events and Trends in Climate and Hydrology*, J. Kropp and H.-J. Schellnhuber Eds. Berlin, Germany: Springer, 2011, pp. 202–213, doi: [10.1007/978-3-642-14863-7_10](https://doi.org/10.1007/978-3-642-14863-7_10).
- [41] W. Zhang, *The Study of High Embankment Settlement Deformation Monitoring and Prediction About the New Airport in Kunming*. Chengdu, China: Chengdu Univ. Technol. Press, 2013.
- [42] C. Xie, H. Liu, and H. Gan, "Study on deformation of ground under high fill of block and detritus," *Chin. J. Geotech. Eng.*, vol. 24, no. 01, pp. 38–41, 2002.
- [43] Z. Liu, *Research on the Stability of the High Fill Slope at the North of the KM New Airport's West Runway*. Chengdu, China: Chengdu Univ. Technol. Press, 2013.
- [44] H. Wang, *Study on the Factors Influencing the Stability of High Fill Slope in Southwest Mountainous Airports*. Chengdu, China: Chengdu Univ. Technol. Press, 2018.
- [45] S. Yue, P. Pilon, and G. Cavadias, "Power of the Mann-Kendall and Spearman's rho tests for detecting monotonic trends in hydrological series," *J. Hydrol.*, vol. 259, no. 1, pp. 254–271, Mar. 2002, doi: [10.1016/S0022-1694\(01\)00594-7](https://doi.org/10.1016/S0022-1694(01)00594-7).
- [46] S. Yue and C. Y. Wang, "Power of the Mann-Whitney test for detecting a shift in median or mean of hydro-meteorological data," *Stochastic Environ. Res. Risk Assessment*, vol. 16, no. 4, pp. 307–323, Aug. 2002, doi: [10.1007/s00477-002-0101-9](https://doi.org/10.1007/s00477-002-0101-9).



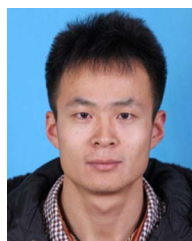
Mingchun Wen received the B.E. degree in civil engineering from Shenzhen University, Shenzhen, China, in 2017. He is currently working toward the M.E. degree in resources and environment from Yunnan University, Kunming, China.

His research interests include algorithm developments for multitemporal InSAR techniques and monitoring the deformation of infrastructures.



Mengshi Yang (Member, IEEE) received the B.E. degree in geomatics engineering from Central South University, Changsha, China, in 2012, and the Ph.D. degree in geodetic engineering from Delft University of Technology, Delft, The Netherlands, in 2020.

Since 2021, she has been an Associate Professor with the Faculty of Earth Sciences, Yunnan University, Kunming, China. Her research interests include the synthetic aperture radar interferometry (InSAR) and InSAR time-series technique for deformation monitoring and interpretation.



Xin Zhao received the M.Eng. degree in physical geography from the Institute of Mountain Hazards and Environment, Chinese Academy of Sciences, Chengdu, China, in 2013. He is currently working toward the Ph.D. degree in cartography and geographical information systems with the Institute of International Rivers and Eco-Security, Yunnan University, Kunming, China.

His current research interests include geological hazard monitoring and evaluation and the evolution of disaster landforms.



Zhifang Zhao received the B.S. degree in geomorphology and quaternary geology from Nanjing University, Nanjing, China, in 1992, and the Ph.D. degree in geological resources and geological engineering, specializing in resource and environment remote sensing, from the China University of Geosciences, Beijing, China, in 2009.

Since 2009, she has been a Professor with the Department of Earth Sciences, Yunnan University, Kunming, China. Her current research focuses on utilizing synthetic aperture radar interferometry (InSAR) for

monitoring geological phenomena deformation and conducting deformation genesis analysis.